Supplementary information

Observations of high time-resolution and size-resolved aerosol chemical composition and microphysics in the central Arctic: implications for climate-relevant particle properties

Benjamin Heutte[1], Nora Bergner[1], Hélène Angot[1,a], Jakob B. Pernov[1], Lubna Dada[1,2], Jessica A. Mirrielees[3], Ivo Beck[1], Andrea Baccarini[1,b], Matthew Boyer[4], Jessie M. Creamean[5], Kaspar R. Daellenbach[2], Imad El Haddad[2], Markus Frey[6], Silvia Henning[7], Tiia Laurila[4], Vaios Moschos[2], Tuukka Petäjä[4], Kerri A. Pratt[3,8], Lauriane L. J. Quéléver[4], Matthew D. Shupe[9,10], Paul Zieger[11,12], Tuija Jokinen[4,13], Julia Schmale[1,*]

[1]Extreme Environments Research Laboratory, Ecole Polytechnique Fédérale de Lausanne (EPFL) Valais Wallis, Sion, Switzerland
[2]Laboratory of Atmospheric Chemistry, Paul Scherrer Institute, Villigen, Switzerland
[3]Department of Chemistry, University of Michigan, Ann Arbor, MI, USA
[4]Institute for Atmospheric and Earth System Research, INAR/Physics, Faculty of Science, University of Helsinki, Helsinki, Finland
[5]Department of Atmospheric Science, Colorado State University, Fort Collins, CO, USA
[6]Natural Environment Research Council, British Antarctic Survey, Cambridge, UK
[7]Leibniz Institute for Tropospheric Research, Leipzig, Germany
[8]Department of Earth & Environmental Sciences, University of Michigan, Ann Arbor, MI USA
[9]Cooperative Institute for Research in Environmental Sciences, University of Colorado, Boulder, CO, USA
[10]Physical Sciences Laboratory, National Oceanic and Atmospheric Administration, Boulder, CO, USA
[11]Department of Environmental Science, Stockholm University, Stockholm, Sweden
[12]Bolin Centre for Climate Research, Stockholm, Sweden
[13]Climate and Atmosphere Research Centre (CARE-C), The Cyprus Institute, Nicosia, Cyprus

[a] Now at: Univ. Grenoble Alpes, CNRS, INRAE, IRD, Grenoble INP, IGE, Grenoble, France
[b] Now at: Laboratory of Atmospheric Processes and their Impacts, Ecole Polytechnique Fédérale de Lausanne (EPFL), Lausanne, Switzerland

Correspondence to: Julia Schmale (julia.schmale@epfl.ch)

S1 Information on the high-resolution time-of-flight aerosol mass spectrometer (AMS) dataset

S1.1 Detection limits of the AMS

35 The detection limits for the five non-refractory chemical species measured with the AMS (i.e., sulfate, nitrate, ammonium, chloride, and organics) were computed using Eq. S1 (Drewnick et al., 2009):

$$DL_n = \frac{3 * SD}{\sqrt{\frac{n}{m}}} \tag{S1}$$

Where DL_n is the detection limit at a time resolution of n min, SD is the standard deviation of the species' mass concentrations during filter period measurements, n is the averaged time resolution, and m is the output time resolution of the instrument (i.e.,

40 60 sec during MOCCHA and 90 sec during MOSAiC). The calculations were done separately for the four different periods discussed in the manuscript (i.e., Aug-Sep, Oct-Dec, Mar-May, and Jun-Jul). Detection limits for all measured species, at the averaged time resolutions of 10 min and 1 h, are given in Table S1, along with the percentage of unpolluted data below the detection limit at 1 h time resolution for each period.

Table S1: Detection limits (DL) for the five main non-refractory species during the different analysis periods, at 10 min / 1 h time
45 **resolutions.** The percentage of unpolluted data below the detection limit at 1 h time resolution is given in parenthesis for each period. The detection limits were calculated as three times the standard deviation of each species' mass concentration during filter period measurements divided by the square root of the averaging time (Eq. S1). Values are given in units of ng/m^3.

	MOCCHA: Aug-Sep	**MOSAiC: Oct-Dec**	**MOSAiC: Mar-May**	**MOSAiC: Jun-Jul**
Sulfate	10 / 4 (19 %)	23 / 9 (5 %)	24 / 10 (1 %)	11 / 5 (13 %)
Nitrate	13 / 5 (25 %)	14 / 6 (1 %)	17 / 7 (0.1 %)	20 / 8 (83 %)
Ammonium	1 / 0.4 (99 %)	2 / 1 (83 %)	5 / 2 (1 %)	-
Chloride	7 / 3 (98 %)	27 / 11 (2 %)	14 / 6 (1 %)	10 / 4 (37 %)
Organics	110 / 45 (42 %)	80 / 33 (17 %)	62 / 25 (2 %)	138 / 56 (9 %)

S1.2 Sea salt detection with the AMS
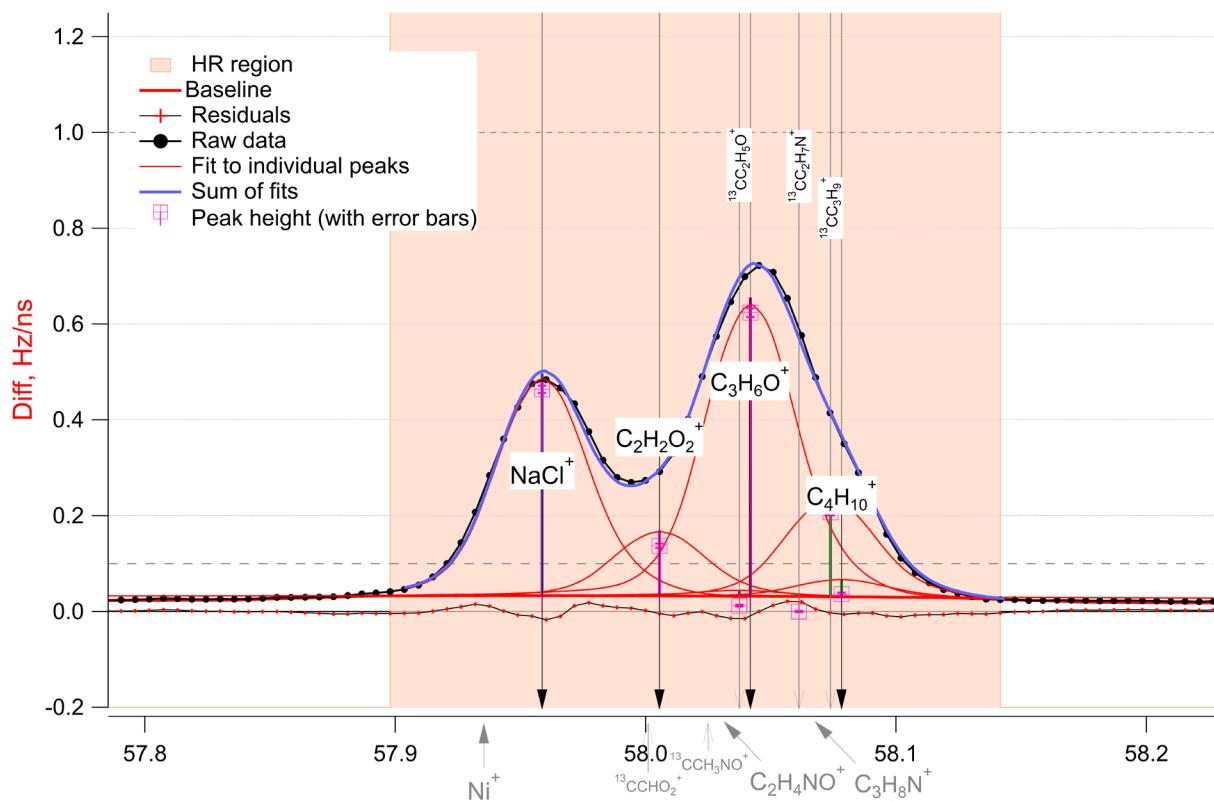
Figure S1: NaCl⁺ peak fitting procedure at *mz* 58. The peak fitting was done using the Peak Integration by Key Analysis (PIKA) v1.25B within the IGOR Pro v9.00 software. The data shown here are of the *difference* signal, which is the difference between the open and closed signal.

50

55

60

S2 Wind speed seasonality
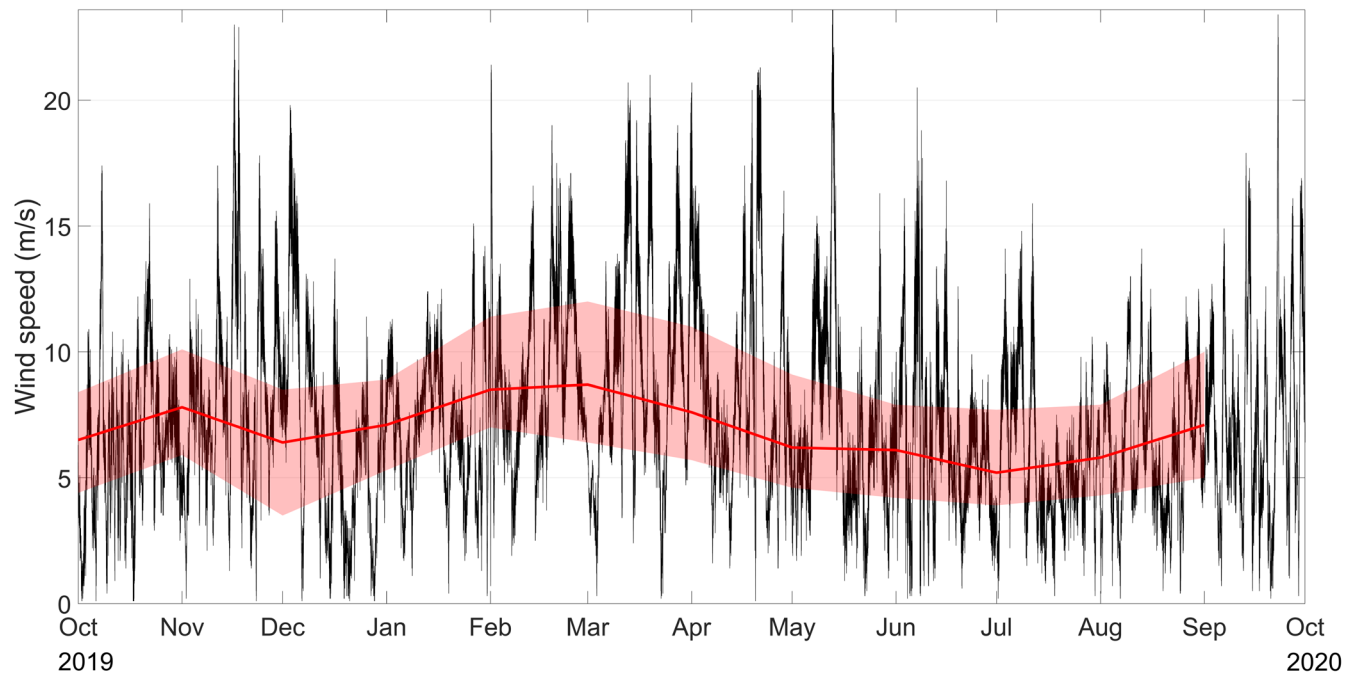
Figure S2: Wind speed annual cycle during MOSAiC. The black lines represent the 1 min wind speed measured onboard Polarstern, while the thick red line correspond to the monthly medians. The shaded red region shows the interquartile range.

65

70

75

S3 High-resolution case studies from November 2019 and March 2020

S3.1 Comparison of sub- and supermicron particle number concentrations
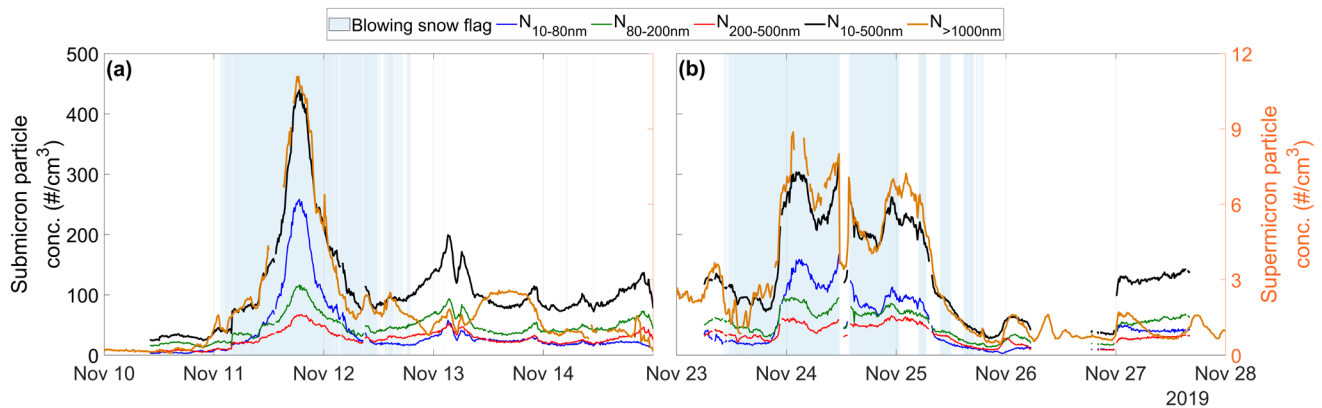
Figure S3: Timeseries of sub- and supermicron particle number concentrations during the (a) November 10th to 15th, 2019 and (b) November 23rd to 28th, 2019 storms. The submicron particle number concentrations were further separated in the size ranges from 10-80 nm, 80-200 nm, and 200-500 nm. For both panels, a blue shading indicates periods when blowing/drfiting snow was detected. All measurements were averaged (arithmetic mean) to 10 min time resolution. Data identified as affected by local contamination (pollution) were removed.
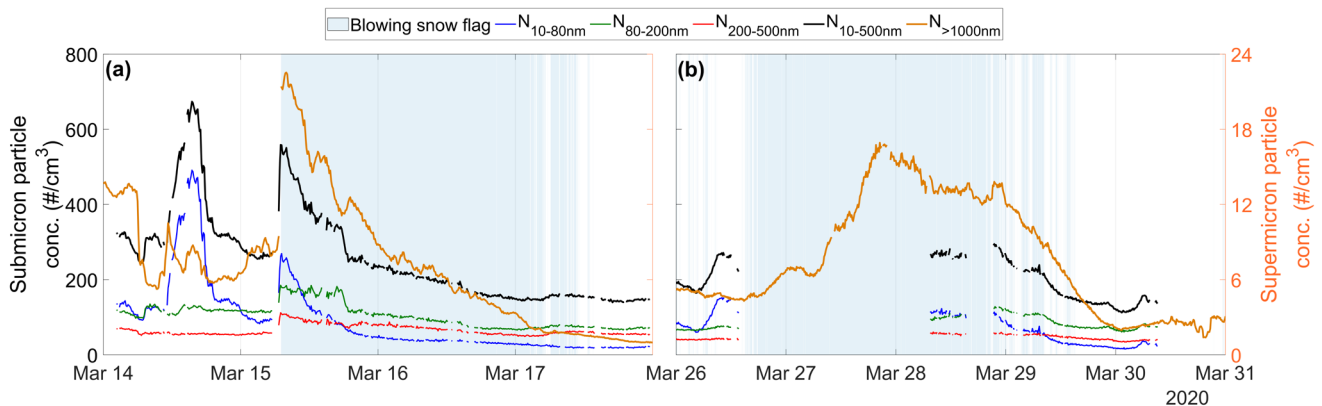
Figure S4: Timeseries of sub- and supermicron particle number concentrations during the (a) March 14th to 18th, 2020 and (b) March 26th to 31st, 2020 storms. The submicron particle number concentrations were further separated in the size ranges from 10-80 nm, 80-200 nm, and 200-500 nm. For both panels, a blue shading indicates periods when blowing snow was detected. All measurements were averaged (arithmetic mean) to 10 min time resolution. Data identified as affected by local contamination (pollution) were removed.

80

S3.2 Source region: FLEXPART back-trajectories

S3.2.1 Method

To identify the source regions of air masses associated with the November (Fig. 5) and March (Fig. 6) storms, we used Lagrangian backward dispersion model simulations from FLEXPART v10.4 (Pisso et al., 2019), performed by the University of Vienna. The simulations were driven by ERA5 meteorological reanalysis data, on a spatial grid with a 0.5° x 0.5° resolution. Every 3 h, along RV *Polarstern*'s track, a cluster of 100,000 particles (passive air tracer) was released and tracked backward in time for 10 days. For our analysis, we summed the residence time of all the particles in each grid cell for the duration of the storm event, when the air had been traveling in the lowest vertical layer of the simulation (i.e., below 100 m). The results of the analysis are shown in Fig. S3 for the two case studies of storms in November and in Fig. S4 for the March storms.

S3.2.2 Back-trajectories for the November 2019 and March 2020 storms
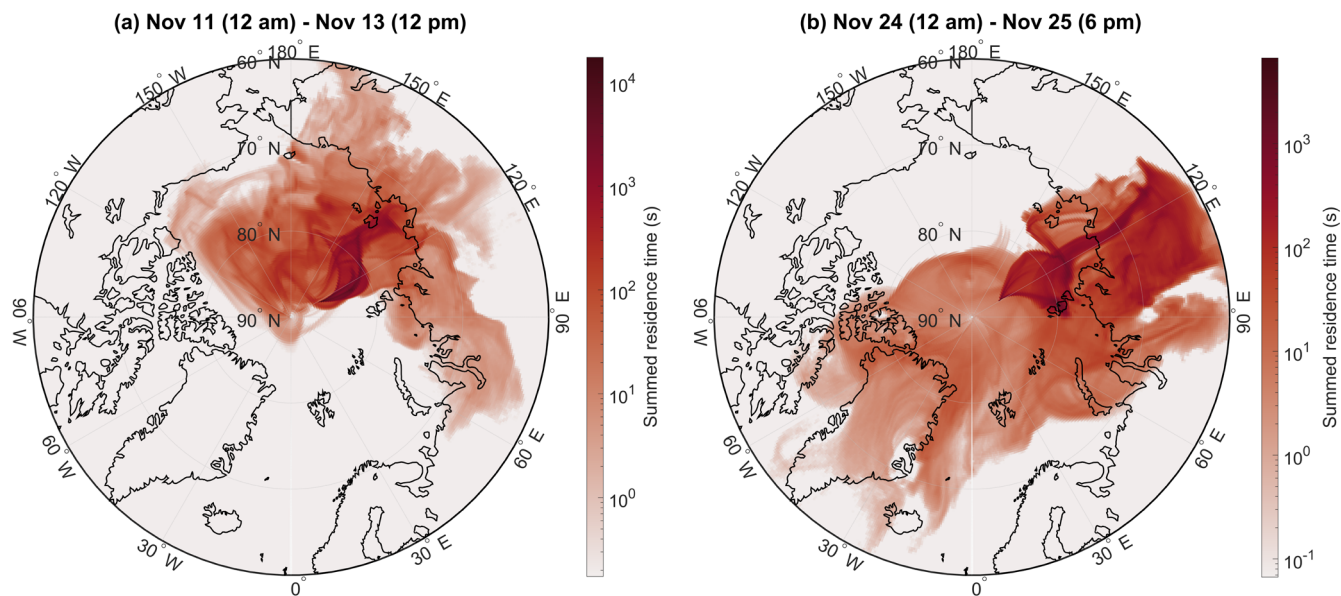
Figure S5: Air-mass back-trajectories during two storms in November 2019, from (a) Nov 11 (12:00 am UTC) to Nov 13 (12:00 pm UTC) and (b) from Nov 24 (12:00 am UTC) to Nov 25 (6:00 pm UTC). The colorscale represent the summed residence time of the particle tracers in each grid cells for the 10-days FLEXPART back-trajectories over the periods of interest.
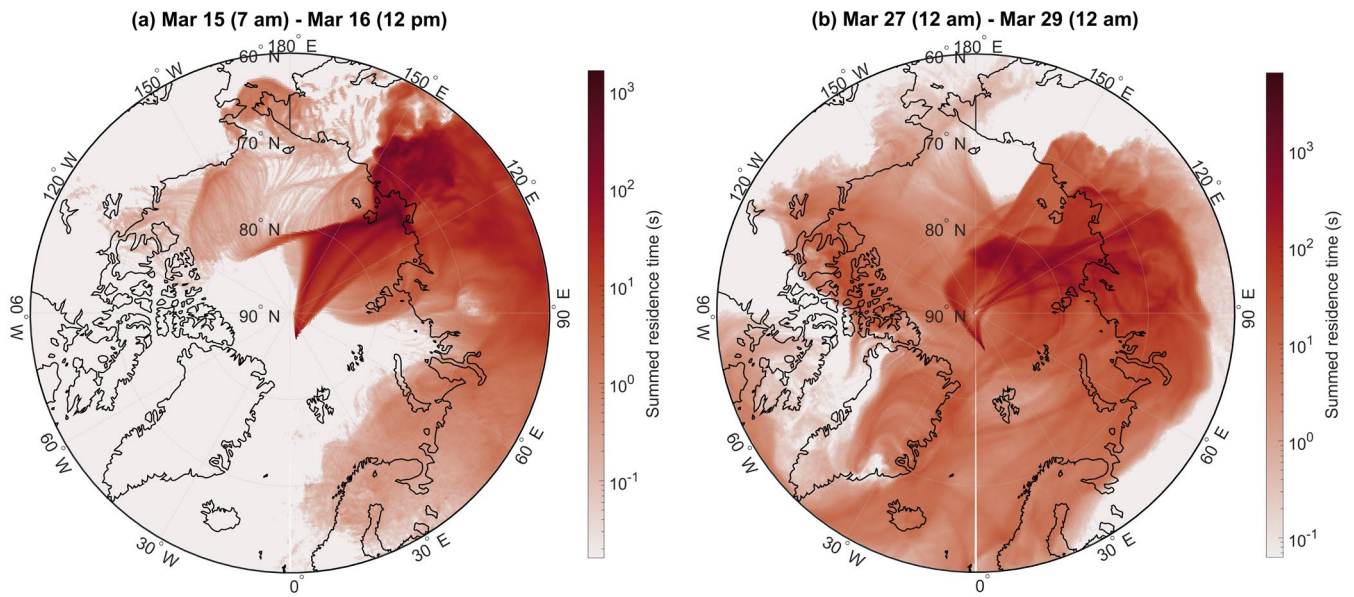
Figure S6: Air-mass back-trajectories during two storms in March 2020, from (a) Mar 15 (7:00 am UTC) to Mar 16 (12:00 pm UTC) and (b) from Mar 27 (12:00 am UTC) to Mar 29 (12:00 am UTC). The colorscale represent the summed residence time of the particle tracers in each grid cells for the 10-days FLEXPART back-trajectories over the periods of interest.

100

105

110

S4 Clustering of the particle number size distributions in autumn and spring

S4.1 Selecting the optimal number of clusters

The number of clusters for the solution was varied from 3 to 30. For each run, the Within-Cluster Sum of Squares (WCSS) was calculated and plotted against the number of clusters (Fig. S7b for Oct-Nov and Fig. S9b for Mar-Apr), and the optimal number of clusters was selected at the estimated inflection point (or "elbow") of the curve. Following this approach, the 8 clusters solution was employed for the October-November period (see Fig. S7a) while the 7 clusters solution was chosen for the March-April period (see Fig. S9a). Adding more clusters didn't yield any significant difference but only isolated particular events with shared characteristics (e.g., two different blowing snow events).

The resulting clusters were further manually merged into 4 clusters for October-November and 3 clusters for March-April based on the similarities of the clusters' median size distribution as well as the potential sources associated with them. Starting with the October-November period, the *blowing snow* (*BLSN*) cluster is solely constituted of Cluster 1 from Fig. S7a. It was named as such given the significantly larger sea salt concentrations associated with this cluster (see Table 1) and appeared to match well with the flagged periods of blowing snow (see Fig. S8) parametrized from snowdrift density and near-surface wind speed observations (Gong et al., 2023). The *long-range transport* (*LRT*) cluster is also solely constituted of Cluster 3, while the *LRT aged* cluster is composed of Clusters 6 and 7, which are characterized by fewer but larger particles. Finally, all clusters with an amplitude of the main (accumulation) mode below 50 cm^{-3} (i.e., Clusters 1, 4, 5, and 8) were grouped into the *background* (*BG*) cluster. For the March-April period, clusters 3 and 7 from Fig. 9a were merged into the spring *BLSN* clusters. Occurrences of the *BLSN* cluster in March-April also matched relatively well with the parametrized blowing snow flag (see Fig. S10). The *haze bimodal* cluster groups all of the original clusters with bimodal median number size distributions (i.e., Clusters 1, 4, and 6). Finally, the very similar Clusters 2 and 5, characterized by monomodal number size distributions and a strong contribution of accumulation mode particles, were grouped into the *haze* cluster.
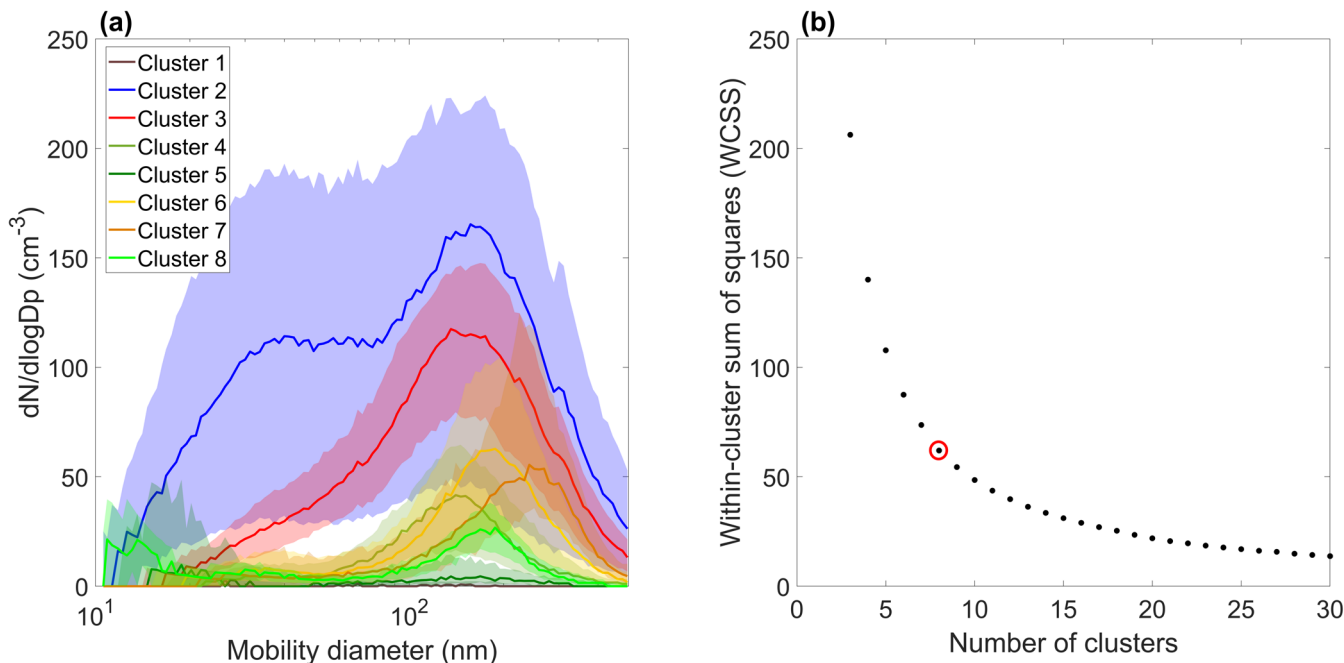
Figure S7: Distributions of the eight PNSD clusters for the October-November period. The median (thick colored lines) and interquartile range (transparent colored envelops) of the eight PNSD clusters are shown in (a). Panel (b) shows the "elbow curve" of the within-cluster sum of squares (WCSS) as a function of the number of clusters, varied from 3 to 30. The red circle outlines the chosen solution (i.e., 8 clusters) at the estimated inflection point of the curve.
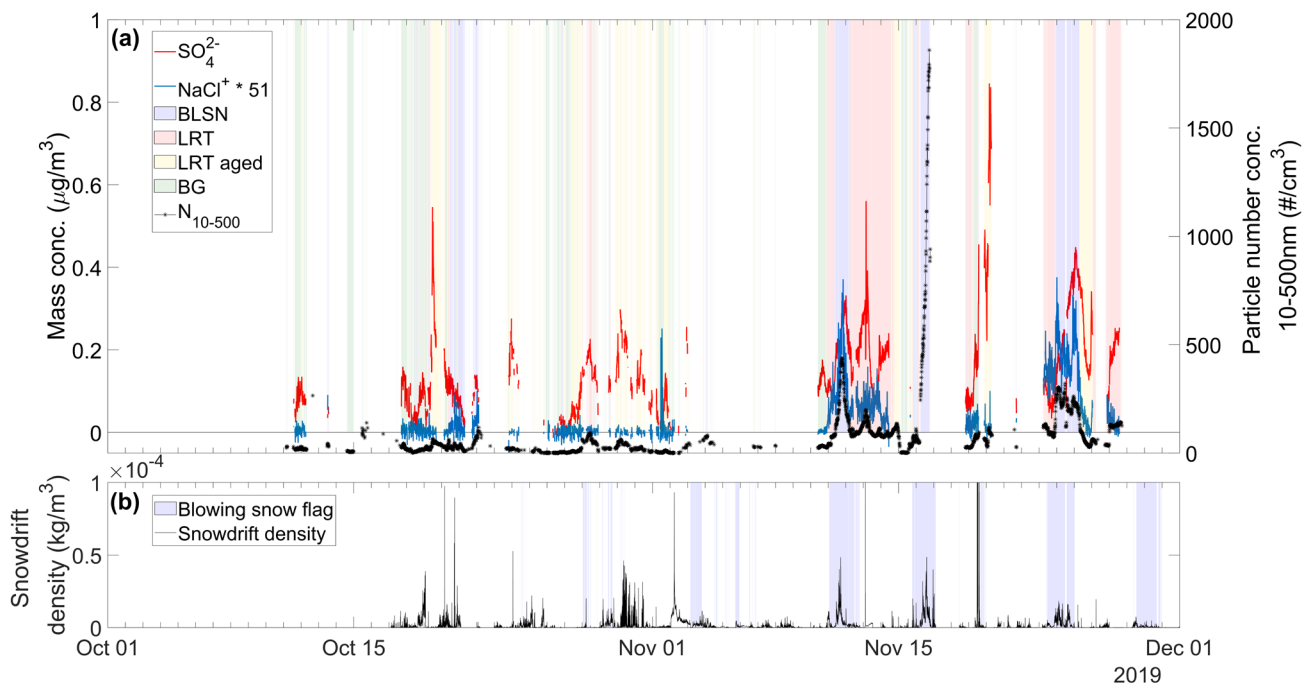
Figure S8: Temporal evolution of the merged PNSD clusters and comparison with the parametrized blowing snow flag for the Oct-Nov 2019 period. For sulfate (SO_4^{2-}) and sea salt (NaCl) only the timesteps where data were available with the SMPS were kept. NaCl mass concentrations are in arbitrary units.
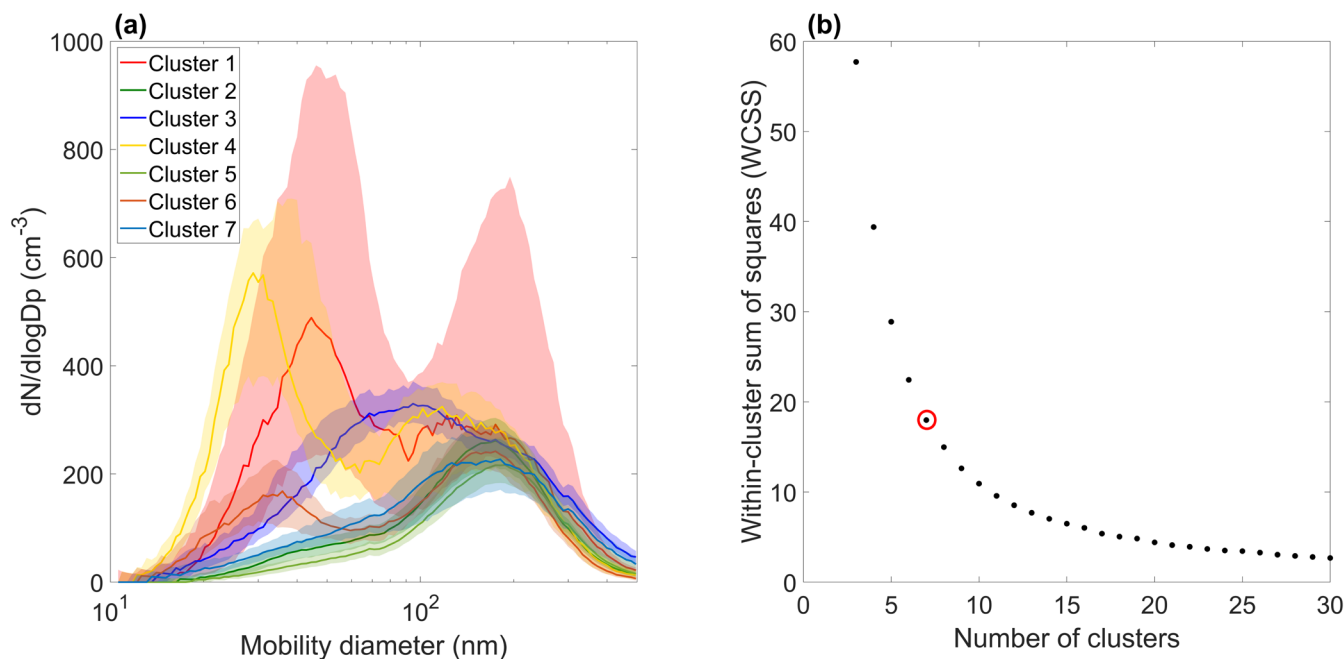
Figure S9: Distributions of the eight PNSD clusters for the March-April period. The median (thick colored lines) and interquartile range (transparent colored envelops) of the eight PNSD clusters are shown in (a). Panel (b) shows the "elbow curve" of the within-cluster sum of squares (WCSS) as a function of the number of clusters, varied from 3 to 30. The red circle outlines the chosen solution (i.e., 7 clusters) at the estimated inflection point of the curve.
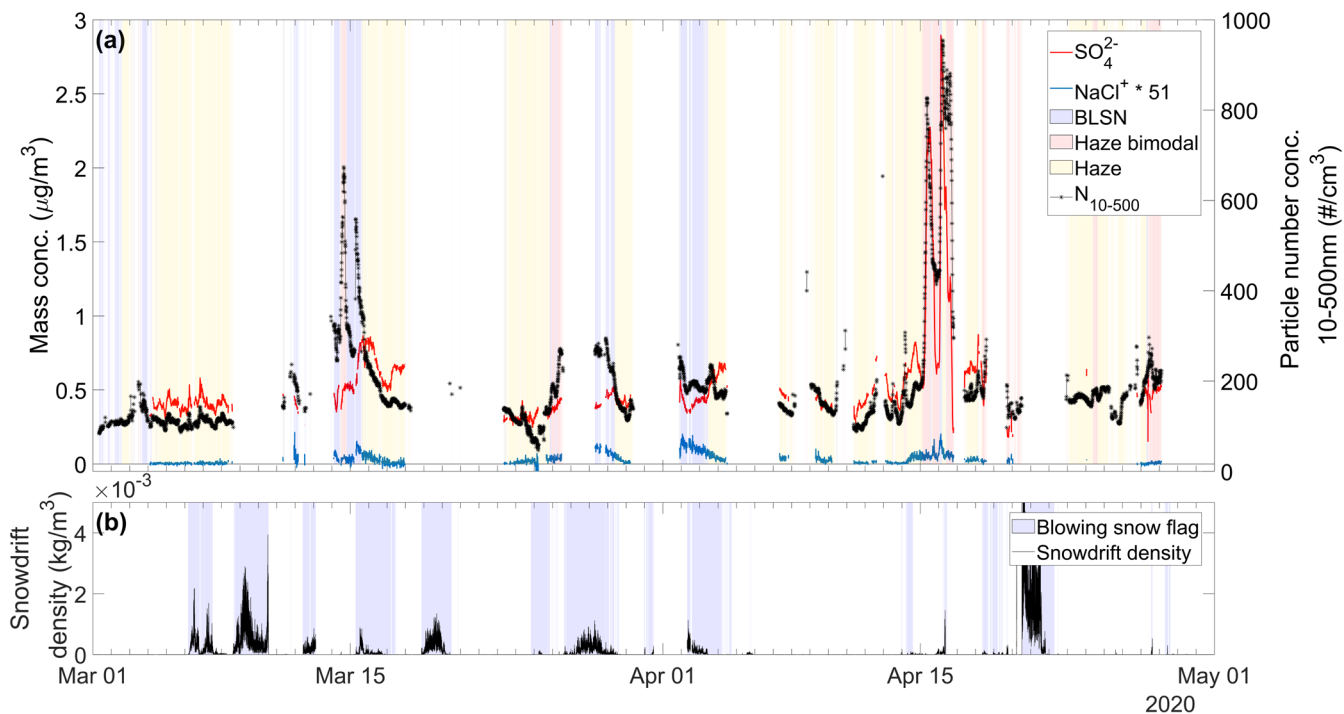
Figure S10: Temporal evolution of the merged PNSD clusters and comparison with the parametrized blowing snow flag for the Mar-Apr 2020 period. For sulfate (SO_4^{2-}) and sea salt (NaCl) only the timesteps where data were available with the SMPS were kept. NaCl mass concentrations are in arbitrary units.
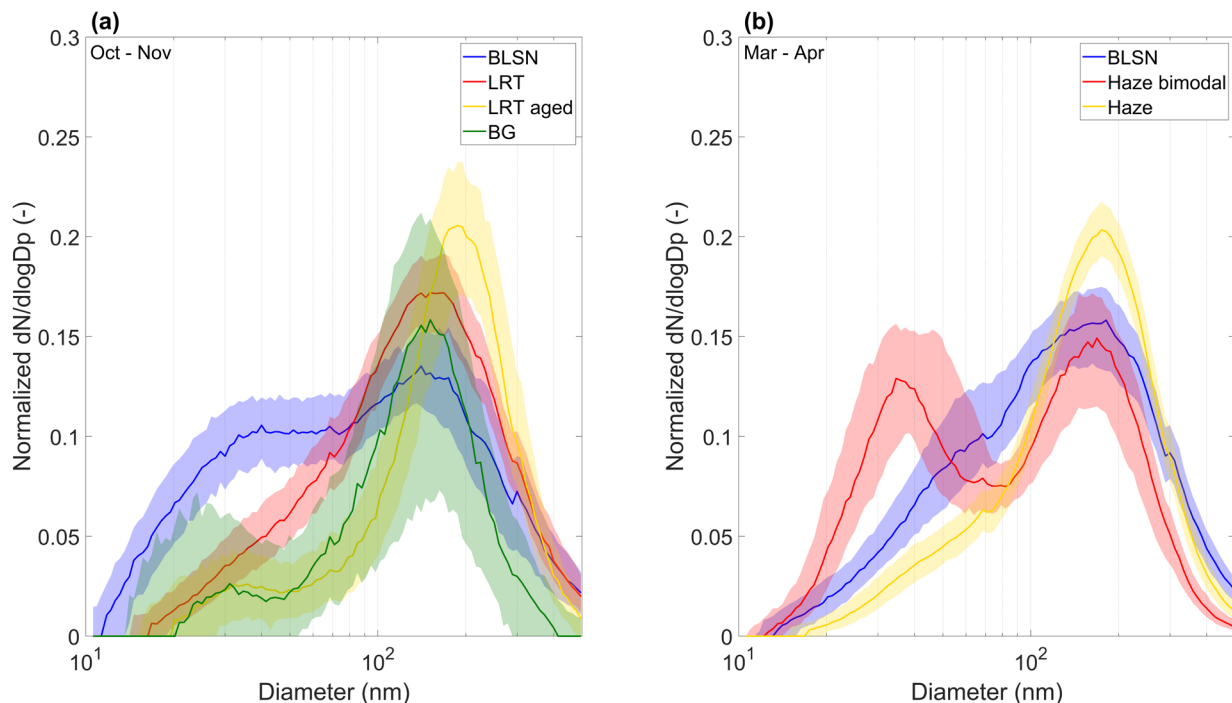
Figure S11: Clustered PNSD in (a) October-November and (b) March-April. This is the same figure as Fig. 7, except that here the number size distributions are normalized to the vector length to compare the shapes of the PNSDs.

140

S4.2 Modal parameters of the cluster's fitted distributions

Table S2: Fitting modal parameters (location of mode and amplitude) for the bimodal log-normal distributions fitted on the median PNSDs of the clusters in Oct-Nov (autumn) and Mar-Apr (spring). The fitting was done using the "Multipeak fitting" package within IGOR Pro v9.02. Errors represent the fitting error and are not a measure of the statistical variance.

	Mode 1		Mode 2	
	Location (nm)	**Amplitude (cm^{-3})**	**Location (nm)**	**Amplitude (cm^{-3})**
BLSN (autumn)	36 ± 1	108.4 ± 1.1	165 ± 2	156.2 ± 1.1
LRT (autumn)	41 ± 1	24.9 ± 0.6	155 ± 1	115.6 ± 0.4
LRT aged (autumn)	44 ± 1	6.9 ± 0.2	192 ± 1	55.4 ± 0.3
BG (autumn)	38 ± 2	3.4 ± 0.2	148 ± 1	16.9 ± 0.2
BLSN (spring)	43 ± 2	70.4 ± 4.2	156 ± 3	245.3 ± 2.9
Haze bimodal (spring)	38 ± 0.2	227.0 ± 1.6	163 ± 1	253.7 ± 1.7
Haze (spring)	57 ± 1	52.0 ± 0.6	176 ± 1	229.3 ± 1.0

145

S5 Size-resolved chemical composition

Table S3: Mode(s) location (in vacuum aerodynamic diameter) for the monthly averaged (median) sulfate and organics mass size distributions. For sulfate, the mode diameters were retrieved by fitting a monomodal log-normal distribution to each monthly mass size distribution**.** Errors represent the fitting error and are not a measure of the statistical variance. For organics, two main modes were observed and the location of the modes were manually estimated.

	Sulfate's mode location (nm)	Organics' modes location (nm)
October	479 ± 3	-
November	500 ± 1	-
March	332 ± 1	$\sim 340 / \sim 820$
April	315 ± 1	$\sim 330 / \sim 840$
May	278 ± 1	$\sim 290 / \sim 840$
June	256 ± 1	-
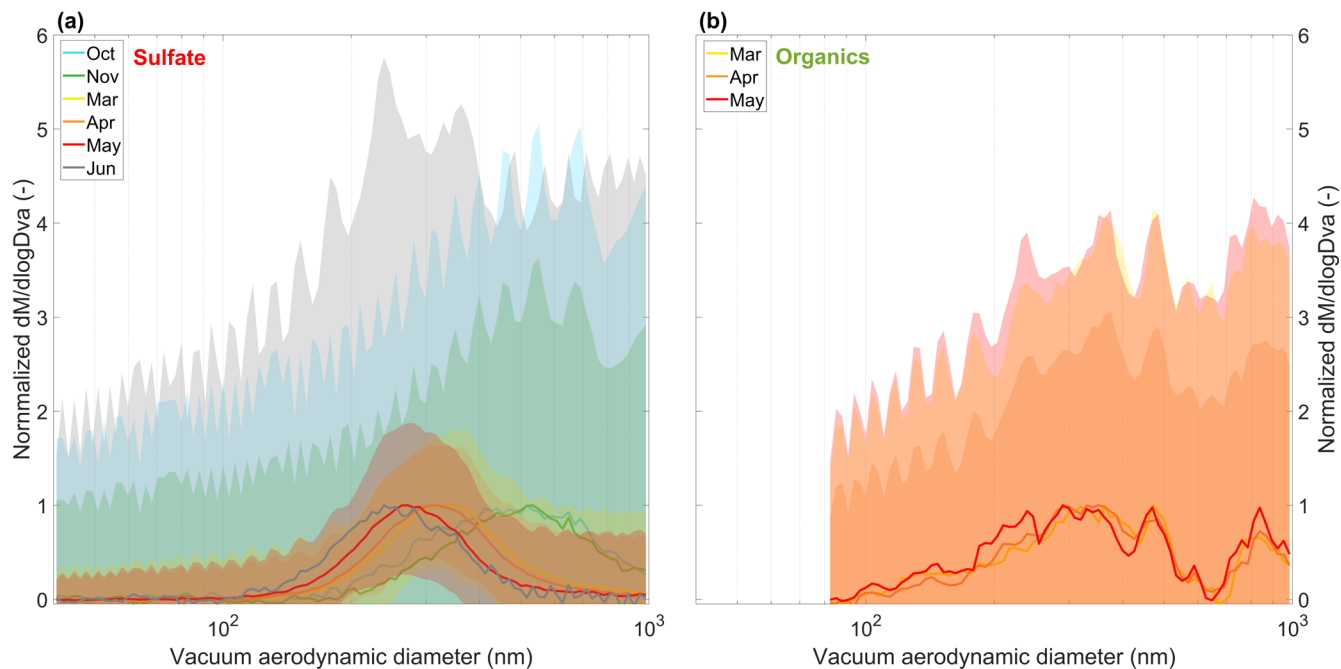
Figure S12: Species-specific size distributions of sulfate (a) and organics (b) during MOSAiC, presented as monthly median values. The thick colored lines represent the medians of the species-specific size distributions, which were normalized by the distributions' maximum value. Shaded regions represent the interquartile range ($25^{th} – 75^{th}$ quantiles) of the distributions, which were also normalized to the maximum of the 50th quantile (median) of the distributions. All the months that are not shown in both panels had a signal-to-noise ratio too low for the PToF data to be analyzed, mainly for organics outside of the spring months. The monthly medians exclude polluted data for both sulfate and organics. Due to gas-phase interactions with the organics' PToF signal, the size distributions of organics in (b) were truncated below 80 nm due to interferences with gas-phase compounds**.**
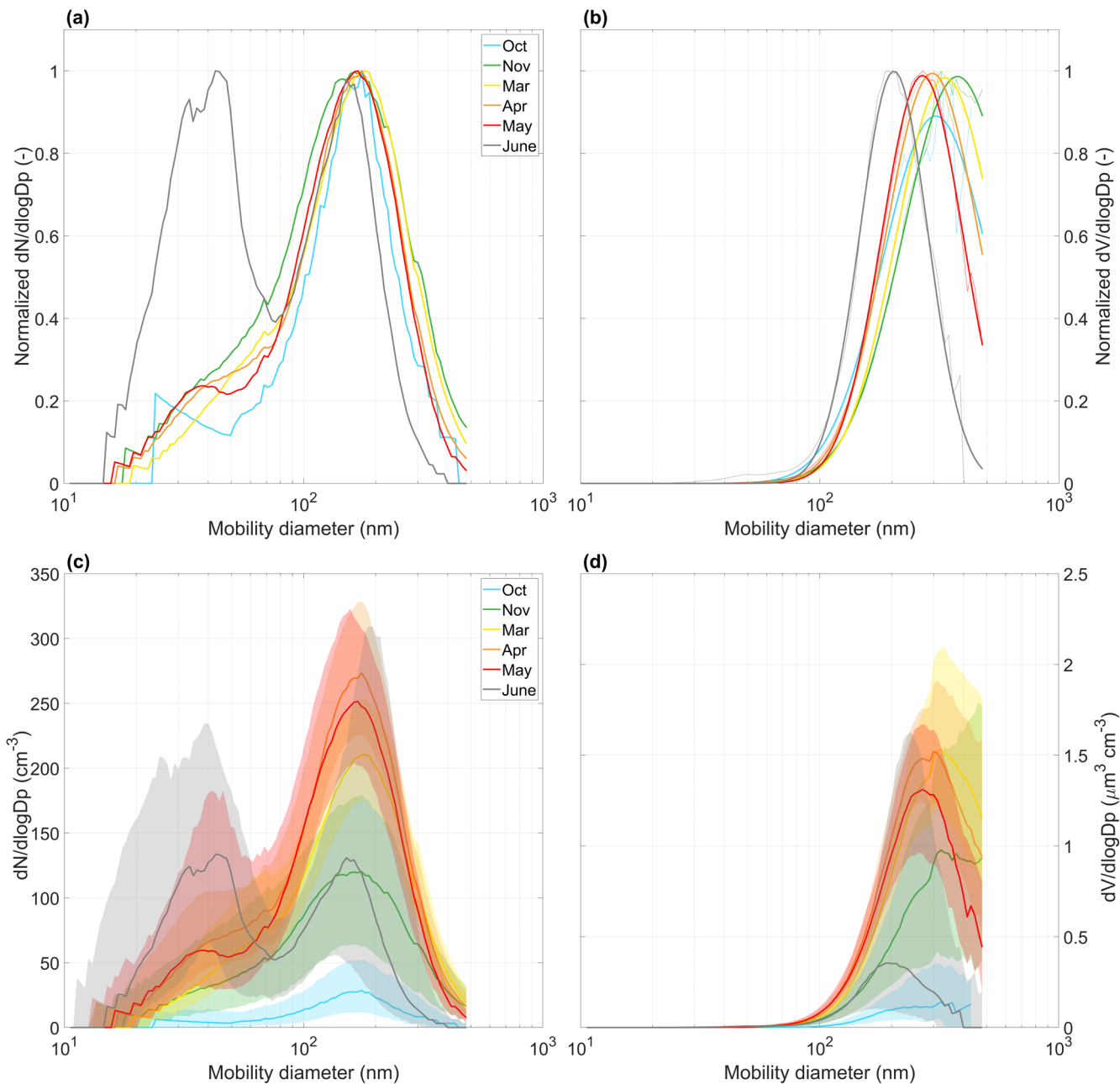
Figure S13: Particle number (a, c) and volume (b, d) size distributions for October, November, March, April, May, and June, during MOSAiC based on SMPS measurements. In panel (a) and (b), the monthly medians were normalized by the distributions' maximum value to compare their shape. The particle volume size distributions in (b) were fitted with monomodal log-normal distributions and resulting mode diameters were found at 305 ± 5, 376 ± 2, 334 ± 1, 295 ± 1, 268 ± 1, and 204 ± 1 nm for Oct, Nov, Mar, Apr, May, and Jun, respectively. In panel (c) and (d), the monthly medians are given as absolute values, where the shaded region represents the interquartile range. Data identified as affected by local contamination were not considered in the computation of the monthly statistics.

155 References

Drewnick, F., Hings, S. S., Alfarra, M. R., Prevot, A. S. H., and Borrmann, S.: Aerosol quantification with the Aerodyne Aerosol Mass Spectrometer: detection limits and ionizer background effects, Atmospheric Measurement Techniques, 2, 33–46, https://doi.org/10.5194/amt-2-33-2009, 2009.

Gong, X., Zhang, J., Croft, B., Yang, X., Frey, M. M., Bergner, N., Chang, R. Y.-W., Creamean, J. M., Kuang, C., Martin, R.
160 V., Ranjithkumar, A., Sedlacek, A. J., Uin, J., Willmes, S., Zawadowicz, M. A., Pierce, J. R., Shupe, M. D., Schmale, J., and Wang, J.: Arctic warming by abundant fine sea salt aerosols from blowing snow, Nat. Geosci., 16, 768–774, https://doi.org/10.1038/s41561-023-01254-8, 2023.

Pisso, I., Sollum, E., Grythe, H., Kristiansen, N. I., Cassiani, M., Eckhardt, S., Arnold, D., Morton, D., Thompson, R. L., Groot Zwaaftink, C. D., Evangeliou, N., Sodemann, H., Haimberger, L., Henne, S., Brunner, D., Burkhart, J. F., Fouilloux, A.,
165 Brioude, J., Philipp, A., Seibert, P., and Stohl, A.: The Lagrangian particle dispersion model FLEXPART version 10.4, Geoscientific Model Development, 12, 4955–4997, https://doi.org/10.5194/gmd-12-4955-2019, 2019.